Cell Reports, Volume *19*

Supplemental Information

Structural Basis of the Human Endoglin-BMP9 Interaction: Insights into BMP Signaling and HHT1

Takako Saito, Marcel Bokhove, Romina Croci, Sara Zamora-Caballero, Ling Han, Michelle Letarte, Daniele de Sanctis, and Luca Jovine

This file includes:

SUPPLEMENTAL FIGURES

SUPPLEMENTAL TABLE

SUPPLEMENTAL EXPERIMENTAL PROCEDURES

SUPPLEMENTAL REFERENCES

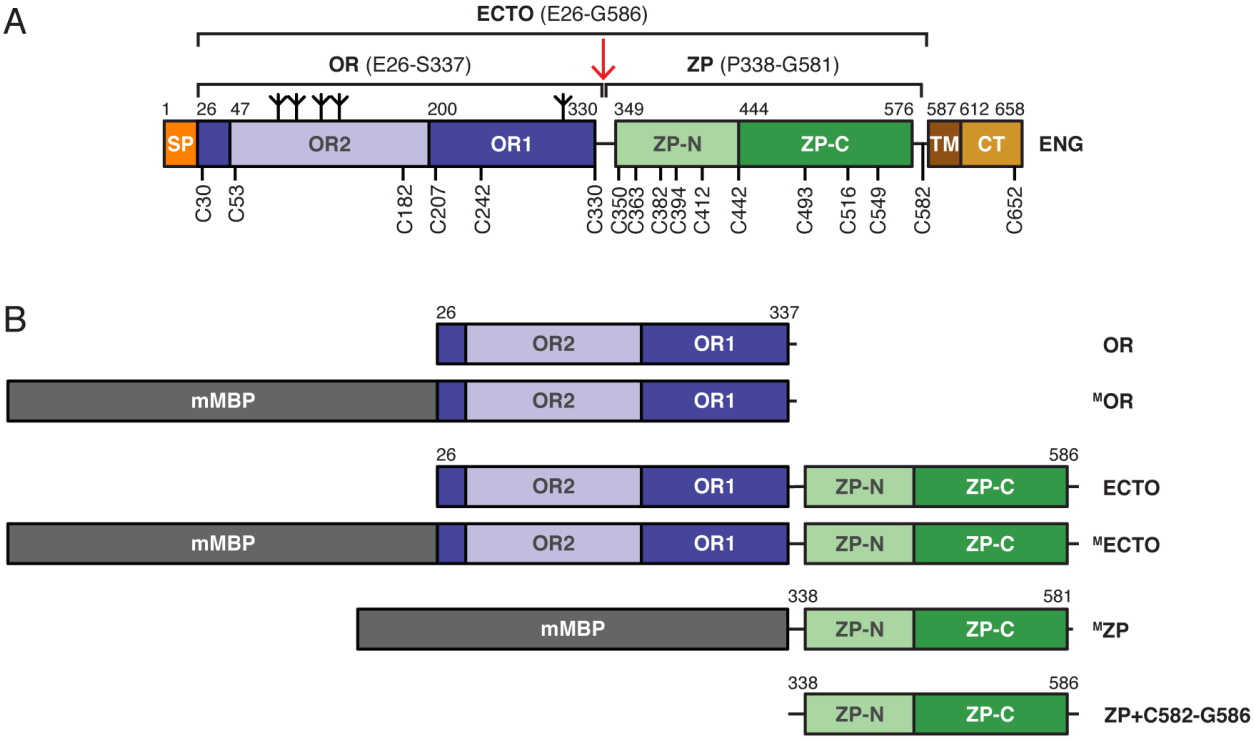
A
ECTO (E26-G586)
OR (E26-S337)
ZP (P338-G581)
1 26 47 200 330 349 444 576 587 612 658
SP
OR2
OR1
ZP-N
ZP-C
TM
CT
ENG
C30 C53 C182 C207 C242 C330 C350 C363 C382 C394 C412 C442 C493 C516 C549 C582 C652
B
26 337
OR2
OR1
OR
mMBP
MOR
26 586
ZP-N
ZP-C
ECTO
MECTO
338 581
MZP
338 586
ZP+C582-G586
C
MORC242S, Δ330-337
26 329
C30 C53 C182 C207 C242
C→S
kDa
MOR
MORC242S, Δ330-337
260
160
110
80
60
50
40
30
20
BMP9

Figure S1. ENG Organization and Expression Constructs. Related to Figures 1, 3 and 4.

(A) Domain architecture of ENG. SP, signal peptide; TM, transmembrane domain; CT, cytoplasmic domain. N-glycosylation sites are indicated by inverted tripods and the OR/ZP interdomain linker is marked by a red arrow.

(B) ENG constructs used for crystallization and functional assays.

(C) Non-reducing SDS-PAGE after BMP9 co-expression followed by His pull-down indicates that both ^{M}OR and $^{M}OR_{C242S,\ \Delta330\text{-}337}$ are secreted as monomers and bind BMP9.

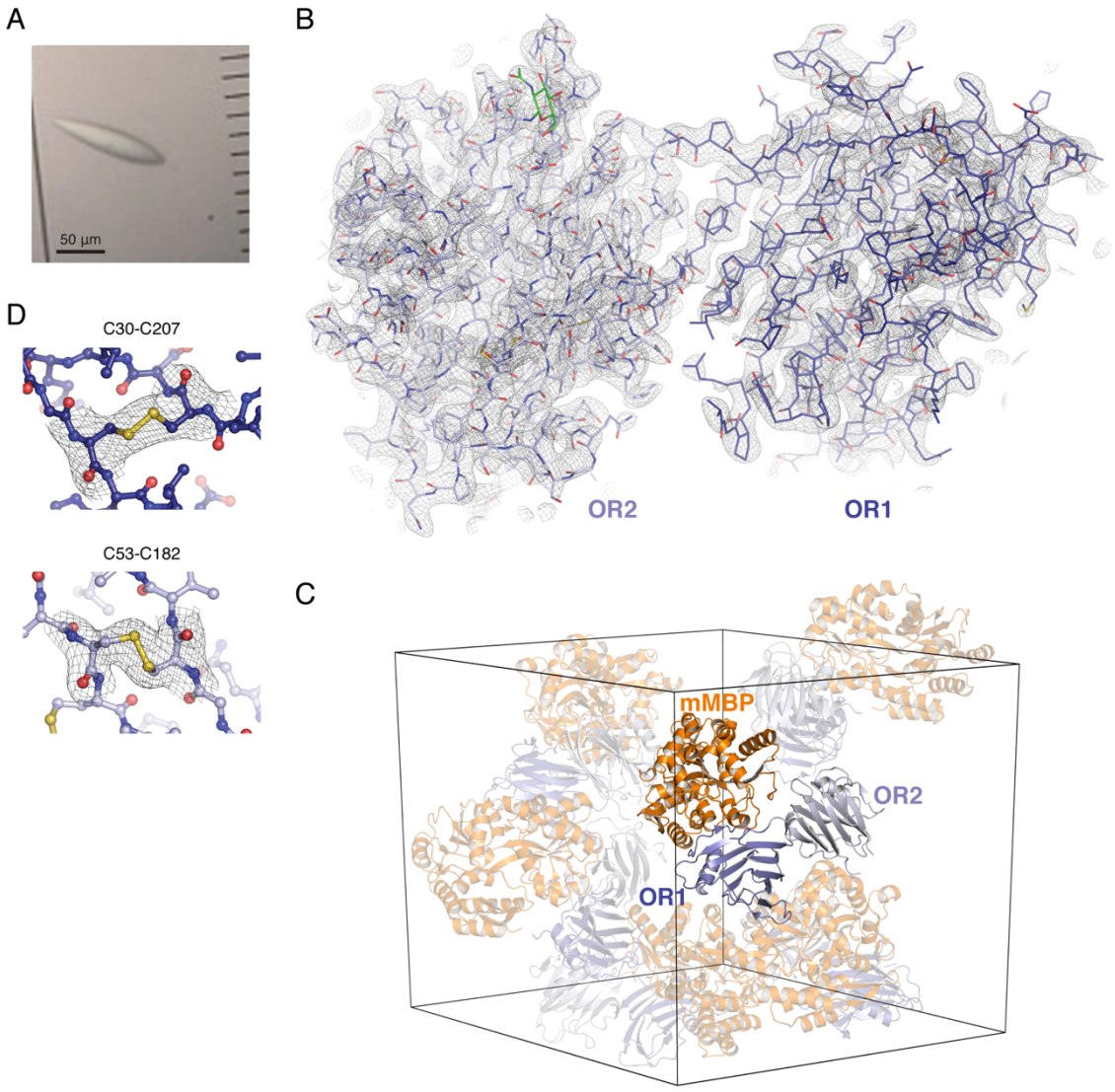
A
50 µm
B
OR2
OR1
C
mMBP
OR2
OR1
D
C30-C207
C53-C182

Figure S2. Crystal Structure of mMBP-Fused ENG OR. Related to Figure 1.

(A) Crystal of ^{M}OR.

(B) Stick representation of ENG OR1 and OR2 domains, colored dark blue and light blue, respectively. The *2mFo-DFc* electron density map contoured at 1.0 σ is shown as a black mesh.

(C) Crystal packing of mMBP-OR. mMBP is orange, OR1 and OR2 are colored as in panel B. The unit cell is shown, and symmetry-related molecules are semi-transparent.

(D) Detail of OR disulfide bonds and corresponding electron density map, using the same representation as in panel B.

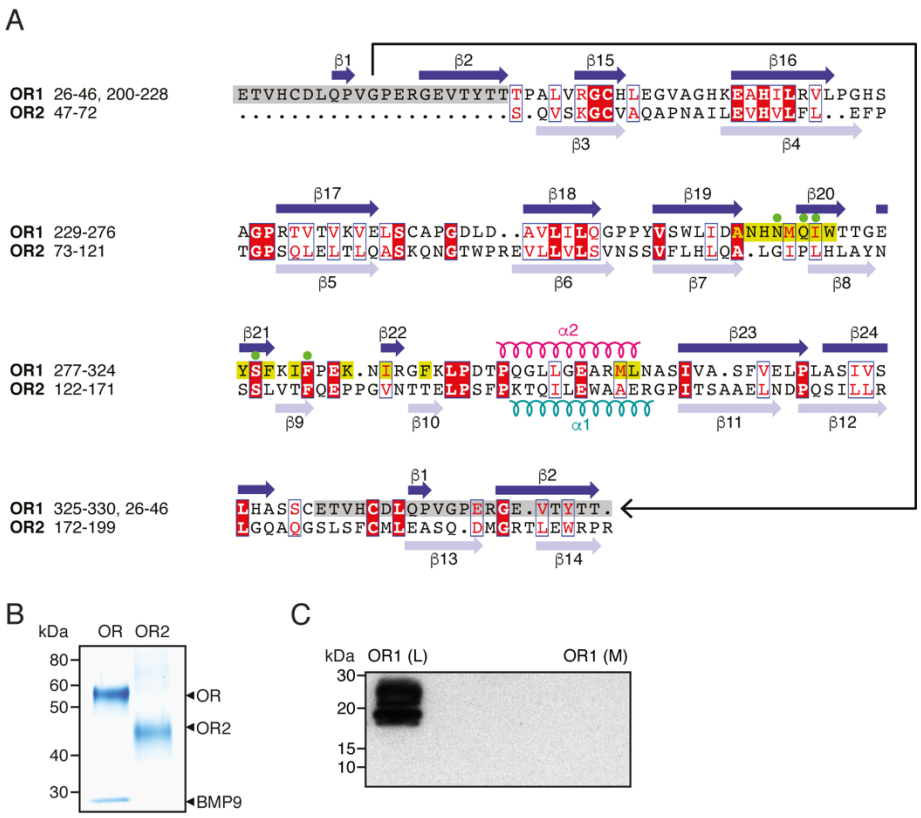

Figure S3. Relationship between OR1 and OR2 and Possible Evolution of ENG OR.

Related to Figure 1.

(A) Structure-based sequence alignment of OR1 and OR2, showing that the N-terminal part of OR1 (gray box) aligns with the C-terminal part of OR2. Secondary structure elements are shown; conserved residues are highlighted in red, residues within 4.5 Å of BMP9 are indicated in yellow and mutagenized sites are marked by green circles.

(B) Coomassie-stained gel of BMP9 pull-down with purified OR or OR2 (ENG T45-L203). BMP9 binds OR but not OR2, narrowing down the ligand binding site to OR1.

(C) Anti-His immunoblot shows that OR1 (ENG E26-T46-$(GGGS)_2$-L203-S329 C242S) is expressed but not secreted by mammalian cells. L, cell lysate; M, conditioned medium.

A

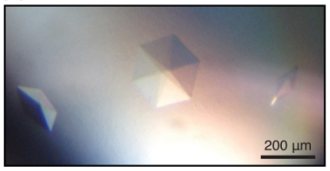

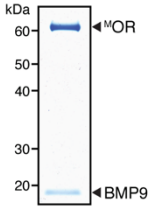

B

Model	R_{work}	R_{free}
MBP	44.5	47.1
MBP OR1	39.0	41.1
MBP OR1 BMP9	34.9	37.0
MBP OR1 BMP9 OR2	30.2	34.3

C

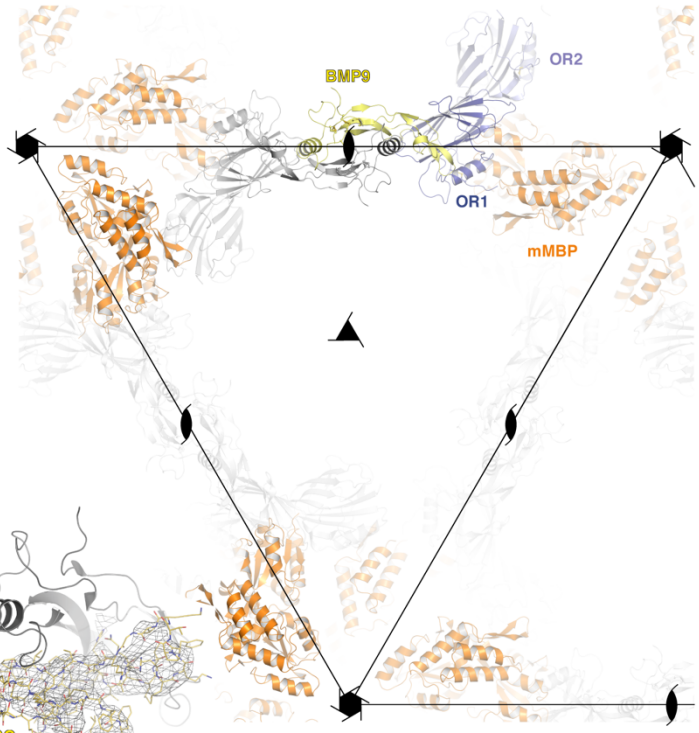

D

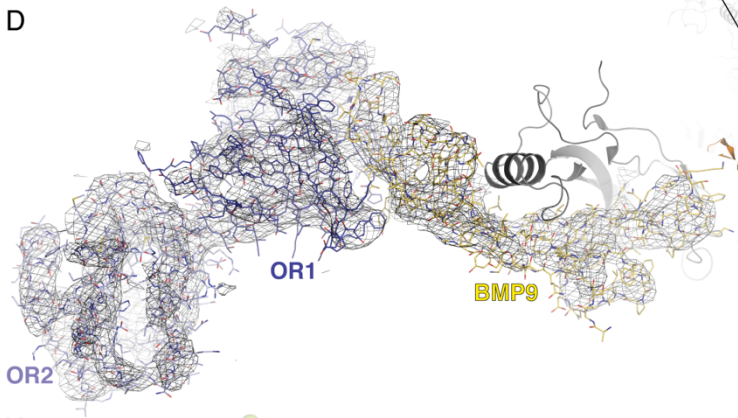

H

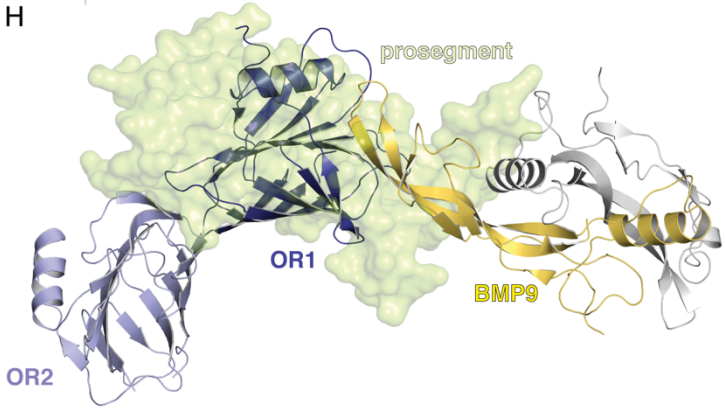

E

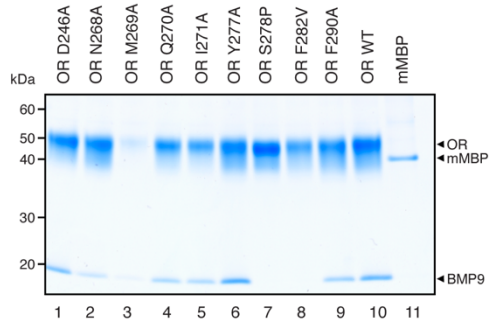

G

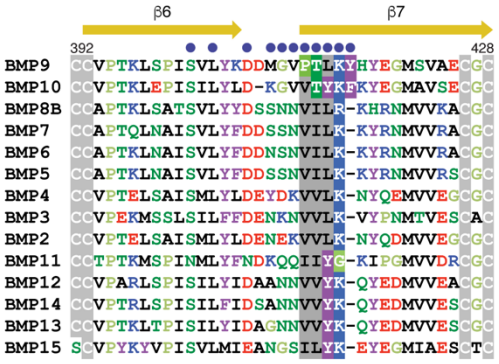

F

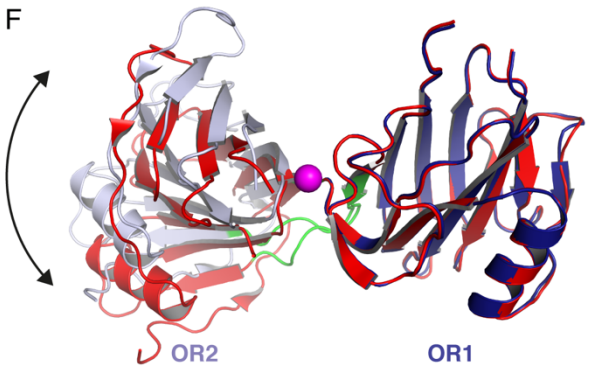

Figure S4. Structure of ENG OR in Complex with BMP9. Related to Figure 2.

(A) Hexagonal crystals of ^{M}OR-BMP9 (left). Despite their perfect shape, the complex crystals diffract very weakly and several hundred specimens were screened in order to obtain the 4.45 Å resolution data used for structure determination. Coomassie-stained SDS-PAGE analysis (right) indicates that the crystals contain both ^{M}OR and BMP9.

(B) Refinement statistics (phenix.refine R-factors) improve when additional model components are added.

(C) Correct placement of the ^{M}OR-BMP9 complex (OR1: dark blue; OR2: light blue; BMP9: yellow) in the unit cell, together with the indicated symmetry elements, generates the typical BMP9 homodimer (grey/yellow). ENG OR and BMP9 molecules in neighboring asymmetric units are shown as transparent light grey cartoons; mMBP moieties are orange. Note how the BMP9-bound mMBP-OR fusion protein packs completely differently from its unbound counterpart (Figure S2C).

(D) *2mFo-DFc* electron density map shown for one asymmetric unit of the complex contoured at 1.0 σ. Proteins are shown in stick representation and colored as in panel C. The second BMP9 molecule of the dimer is grey.

(E) Coomassie-stained SDS-PAGE analysis of BMP9 pull-down by non-mMBP-fused, C-terminally 6His-tagged OR and mutants thereof. A single batch of conditioned medium from HEK293T cells transfected with BMP9 alone was used as input for all pull-down experiments; C-terminally 6His-tagged mMBP was used as a negative control.

(F) Comparison of free and BMP9-bound OR structures (dark blue/light blue and red, respectively) reveals a ~20-degree rotation of OR2 relative to OR1. Bending residues

(Y44-T46, W196-V204) are green and the rotation axis, which is perpendicular to the plane of the page, is magenta.

(G) Sequence alignment of human BMPs. Secondary structure is marked; residues within 4.5 Å of ENG are indicated with blue circles.

(H) Superposition of the BMP9 precursor (Mi et al., 2015) with BMP9 bound to ENG OR indicates that the prosegment of the precursor is not compatible with ENG binding. OR-BMP9 is oriented as in panel D, with OR1, OR2 and mature BMP9 colored as in panels C and D. The BMP9 prosegment is shown as a yellow surface.

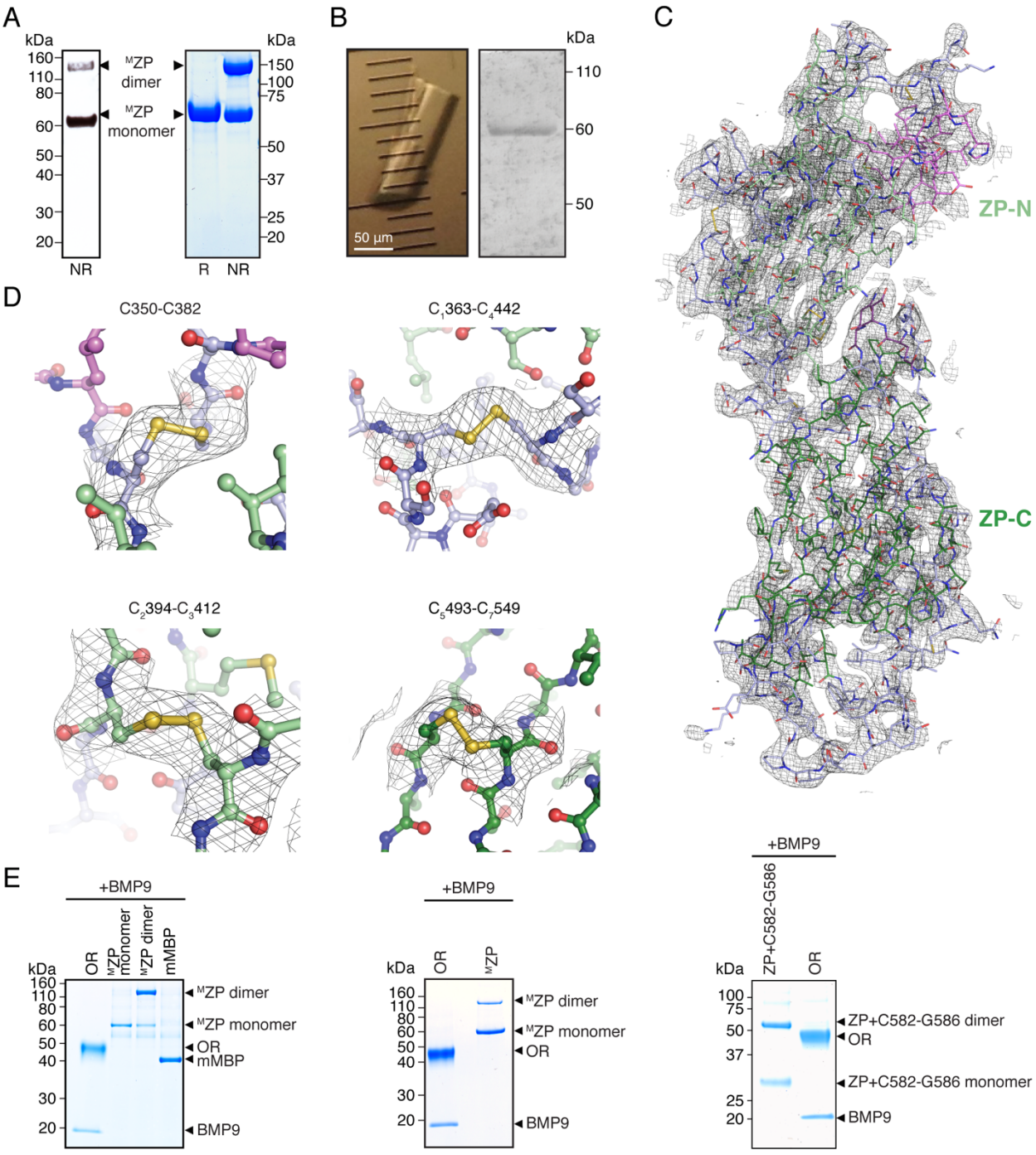
A
kDa
160
110
80
60
50
40
30
20
MZP dimer
MZP monomer
NR
R NR
150
100
75
50
37
25
20
B
kDa
110
60
50
50 µm
C
ZP-N
ZP-C
D
C350-C382
C1363-C4442
C2394-C3412
C5493-C7549
E
+BMP9
OR
MZP monomer
MZP dimer
mMBP
MZP dimer
MZP monomer
OR
mMBP
BMP9
MZP
ZP+C582-G586
ZP+C582-G586 dimer
ZP+C582-G586 monomer

Figure S5. Crystal Structure of ENG ZP. Related to Figure 3.

(A) Anti-His immunoblot of ^{M}ZP secreted in conditioned medium and Coomassie-stained SDS-PAGE of purified ^{M}ZP. Although the protein is mostly secreted as a monomer (see also Figure 4B, lane 2), after concentration it is present as a roughly equimolar mixture of monomer and intermolecularly disulfide-bonded homodimer.

(B) Crystal of ^{M}ZP and non-reducing silver-stained SDS-PAGE analysis of washed ^{M}ZP crystals, indicating that they only consist of monomeric protein.

(C) *2mFo-DFc* electron density map of ZP contoured at 1.0 σ. The model is shown as sticks. Loops are light blue; ZP-N strands and helices are pale green and pink, respectively; ZP-C strands are dark green.

(D) Details of ENG ZP disulfide bonds, represented as in Figure S2D and colored as in panel B. Both signature ZP module disulfides (C_1-C_4, C_2-C_3 and C_5-C_7) and the additional disulfide found in ZP-N (C350-C382) are shown.

(E) In contrast to ^{M}OR, ^{M}ZP does not bind BMP9, as indicated by a pull-down with IMAC and SEC-purified monomeric and dimeric ^{M}ZP (left) or co-expression followed by IMAC pull-down (middle). mMBP does not interfere with a possible interaction between ZP and BMP9, because co-expression of unfused ZP+C582-G586 and BMP9 followed by His pull-down also does not detect binding between the proteins (right).

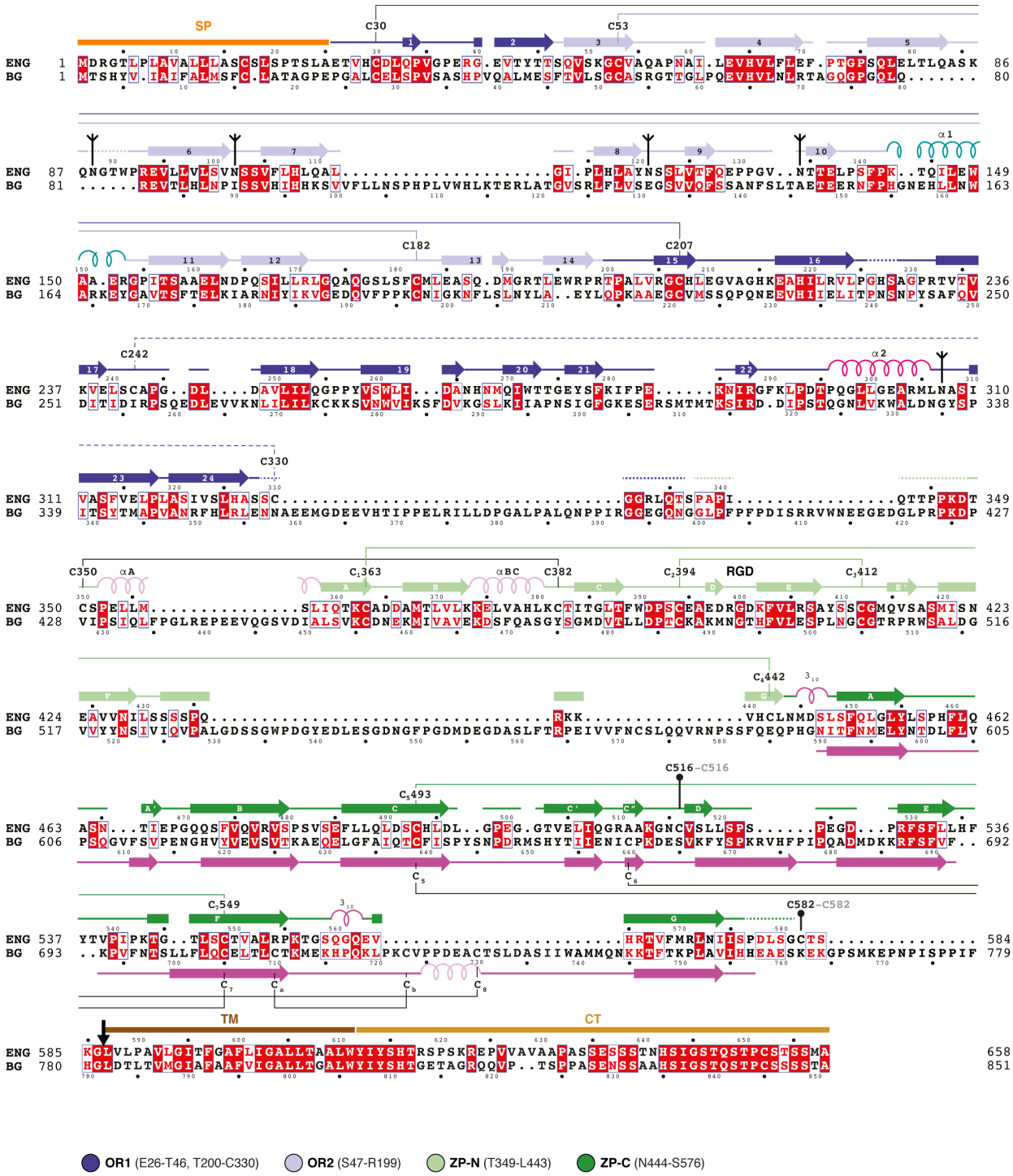
SP
C30
C53
C182
C207
C242
C330
C350
αA
C1363
αBC
C382
C2394
RGD
C3412
C4442
C516–C516
C5493
C7549
C582–C582
TM
CT
ENG 1 MDRGTLPLAVALLLASCSTSPTSLAETVHCDLQPVGPERG.EVTYTTSQVSKGCVAQAPNAI.LEVHVLFLEF.PTGPSQLELTLQASK 86
BG 1 MTSHYV.IAIFALMSFC.LATAGPEPGALCELSPVSASHPVQALMESFTVLSGCASRGTTGLPQEVHVLNLRTAGQGPGQLQ..... 80
ENG 87 QNGTWPREVLLVLSVNSSVFLHLQAL.....GI.PLHLAYNSSLVTFQEPPGV..NTPELPSFPK..TQILEW 149
BG 81 .....REVTLHLNPISSVHIHHKSVVFLLNSPHPLVWHLKTERLATGVSRLFLVSEGSVVQFSSANFSLTAETEERNFPHGNEHLLNW 163
ENG 150 AA.ERGPITSAAELNDPQSTLLRLGQAQGSLSFCMLEASQ.DMGRTLEWRPRTPALVRGCHLEGVAGHKEAHILRVLPGHSAGPRTVTV 236
BG 164 ARKEYGAVTSFTELKIARNNIYIKVGEDQVFPPKCNIGKNFLSLNYLA..EYLQPKAAEGCVMSSQPQNEEVHIIELITPNSNPYSAFQV 250
ENG 237 KVEISCAPG..DL....DAVLILQGPPYVSWLI...DANHNMQIWTTGEYSFKIFPE.....KNIRGFKLPDTPQGLLGEARMLNASI 310
BG 251 DITIDIRPSQEDLEVVKNLILILKCKKSVNWVIKSFDVKGSLKIIAPNSIGFGKESERSMTMTKSIRD.DIPSTQGNLVKWALDNGYSP 338
ENG 311 VASFVELPLASIVSLHASSC.....GGRLQTSPAPI.....QTTPPKDT 349
BG 339 ITSYTMAPVANRFHLRLENNAEEMGDEEVHTIPPELRILLDPGALPALQNPPIRGGEGQNGGLEFPFPDISRRVWNEEGEDGLPRPKDP 427
ENG 350 CSPELLM.....SLIQTKCADDAMTLVLKKELVAHLKCTITGLTFWDPSCEAEDRGDKFVLRSAYSSCGMQVSASMISN 423
BG 428 VIPSIQLFPGLREPEEVQGSVDIALSVKCDNEKMIVAVEKDSFQASGYSGMDVTLLDPTCKAKMNGTHFVLESPLNGCGTRPRWSALDG 516
ENG 424 EAVVNILSSSSRQ.....RKK.....VHCLNMDSLSFQLGLYLSPHFLQ 462
BG 517 VVYYNSIVIQVPALGDSSGWPDGYEDLESGDNGFPGDMDEGDASLFTRPEIVVFNCSLQQVRNPSSFQEQPHGNITFNMELYNTDLFLV 605
ENG 463 ASN...TIEPGQQSFVQVRVSPSVSEFLLQLDSCHLDL..GPEG.GTVELIQGRAAKGNCVSLLSPS.....PEGD...PRFSFLLHF 536
BG 606 PSQGVFSVPENGHVYVEVSVTKAEQELGFAIQTCFISPYSNPDRMSHYTIIENICPKDESVKFYSPKRVHFPIPQADMDKKRFSFVF.. 692
ENG 537 YTVPIPKTG..TLSCTVALRPKTGSQGQEV.....HRTVFMRLNITSPDLSGCTS..... 584
BG 693 ..KPVFNTSLLFLQCELTLCTKMEKHPQKLPKCVPPDEACTSLDASIIWAMMQNKKTFTKPLAVIHHEAESKEKGPSMKEPNPISPPIF 779
ENG 585 KGLVLPAVLGITFGAFLIGALLTAALWYIYSHTRSPSKREPVVAVAAPASSESSSTNHSIGSTQSTPCSTSSMA 658
BG 780 HGLDTLTVMGIAFAAFVIGALLTGALWYIYSHTGETAGRQQVP..TSPPASENSSAAHSIGSTQSTPCSSSSTA 851
OR1 (E26-T46, T200-C330)
OR2 (S47-R199)
ZP-N (T349-L443)
ZP-C (N444-S576)

Figure S6. Sequence Alignment of Human ENG and BG. Related to Figures 1, 3 and 4.

Conserved cysteine residues and experimentally determined secondary structure elements are indicated (human ENG: this work; rat BG ZP-C domain: Lin et al., 2011). The ENG signal peptide and transmembrane domain are indicated by an orange line and a brown line, respectively; the MMP-14 cleavage site (Hawinkels et al., 2010) is indicated by a black arrow. Inverted tripods and lollipops represent ENG N-glycans and Cys residues involved in the C516-C516 and C582-C582 intermolecular disulfides of homodimeric ENG, respectively. Dashed lines within the secondary structure indicate residues that are included in the crystallized constructs but are not resolved in the corresponding electron density maps.

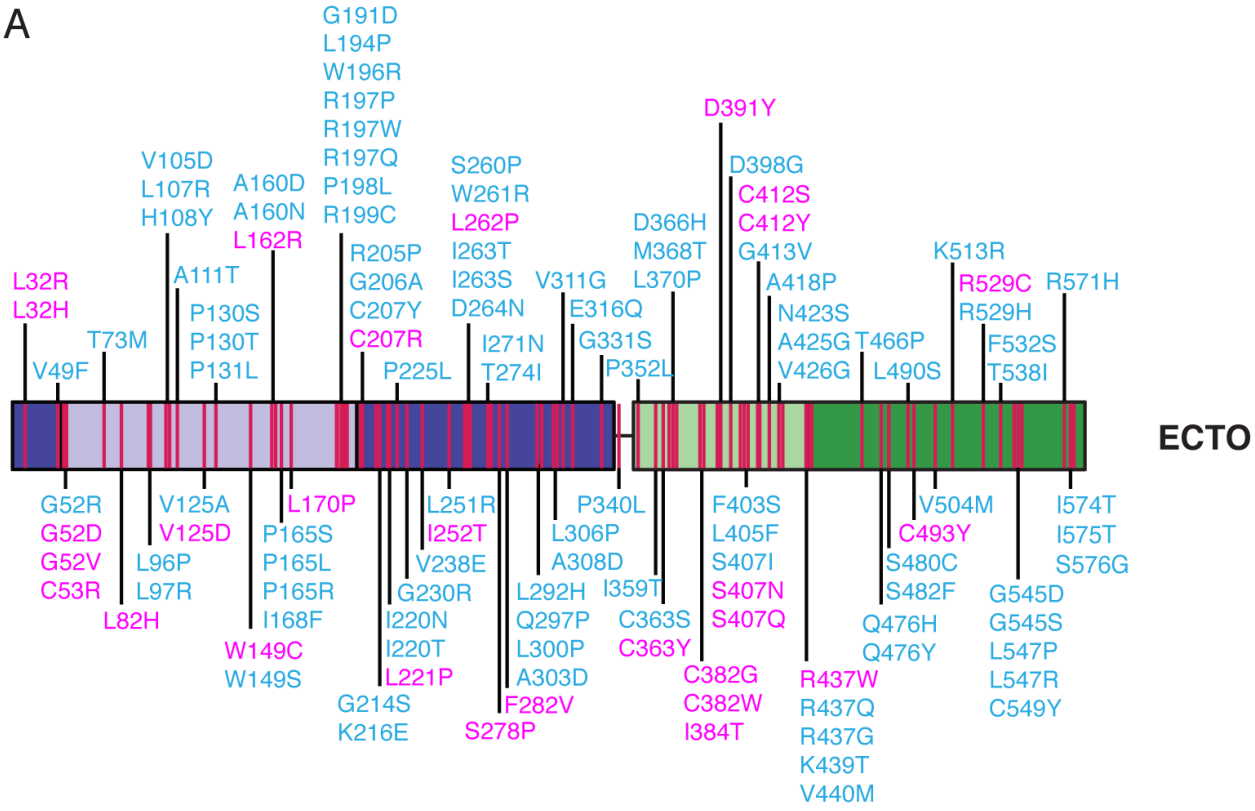
A
G191D
L194P
W196R
R197P
R197W
R197Q
P198L
R199C
V105D
L107R
H108Y
A160D
A160N
L162R
S260P
W261R
L262P
I263T
I263S
D264N
D391Y
D398G
C412S
C412Y
G413V
D366H
M368T
L370P
K513R
R529C
R529H
R571H
F532S
T538I
L32R
L32H
T73M
V49F
A111T
P130S
P130T
P131L
R205P
G206A
C207Y
C207R
P225L
I271N
T274I
V311G
E316Q
G331S
P352L
A418P
N423S
A425G
V426G
T466P
L490S
ECTO
G52R
G52D
G52V
C53R
L82H
L96P
L97R
V125A
V125D
W149C
W149S
P165S
P165L
P165R
I168F
L170P
G214S
K216E
I220N
I220T
L221P
L251R
I252T
V238E
G230R
S278P
L292H
Q297P
L300P
A303D
F282V
L306P
A308D
P340L
I359T
C363S
C363Y
C382G
C382W
I384T
F403S
L405F
S407I
S407N
S407Q
R437W
R437Q
R437G
K439T
V440M
Q476H
Q476Y
V504M
C493Y
S480C
S482F
I574T
I575T
S576G
G545D
G545S
L547P
L547R
C549Y
B
OR2
OR1
ZP-N
ZP-C

Figure S7. Mapping of HHT1 Missense Mutations onto the Structure of ENG. Related to Figure 6.

(A) Domain architecture of ENG, showing the location of missense mutations associated with HHT1 (Ali et al., 2011; Cymerman et al., 2003; Mallet et al., 2014; Paquet et al., 2001; Pece-Barbara et al., 1999; University of Utah Department of Pathology HHT and ENG database). Mutations discussed in the main text and/or included in Figure 6 are highlighted in magenta.

(B) Mapping of the mutations listed in panel A onto a model of full-length ENG, with the same relative orientation of OR and ZP as in Figure 4F. The structure of ENG is shown both in cartoon (left) and surface (right) representations, with mutation sites colored as in panel A.

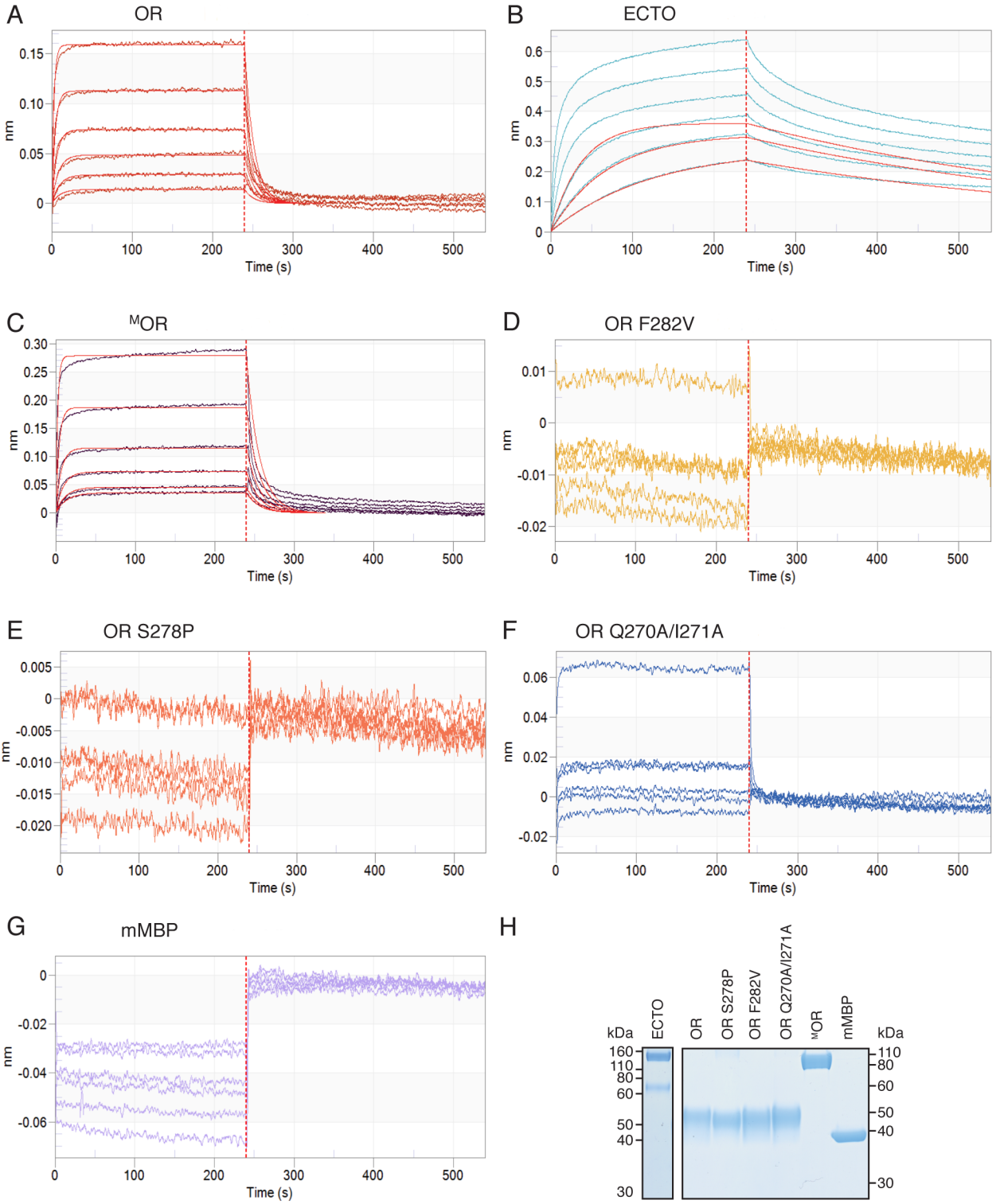
A
OR
B
ECTO
C
MOR
D
OR F282V
E
OR S278P
F
OR Q270A/I271A
G
mMBP
H
nm
Time (s)
kDa
ECTO
OR
OR S278P
OR F282V
OR Q270A/I271A
MOR
mMBP
160
110
80
60
50
40
30

Figure S8. BLI Curve Fitting. Related to Table 1.

(A-G) Association and dissociation curves for the interaction of OR (A), ECTO (B), ^{M}OR (C), OR F282V (D), OR S278P (E) OR Q270A/I271A (F) and mMBP (G) with BMP9 obtained by BLI. Kinetic parameters for the interaction (K_D, k_{on} and k_{off}) were determined by global fitting (red curves) using 1:1 stoichiometry.

(H) Non-reducing SDS-PAGE analysis of purified proteins used for BLI measurements.

Table S1. X-Ray Data Collection and Refinement Statistics. Related to Figures 1-3.

Crystal **PDB ID**	**ENG OR** **5I04**	**BMP9** **5I05**	**ENG OR-BMP9 Complex** **5HZW**	**ENG ZP** **5HZV**
Experiment				
Beamline	ESRF ID29	DLS I02	DLS I02	ESRF ID23-1
Wavelength, Å	0.9762	0.9795	0.9794	1.0000
Number of crystals	1	1	1	1
Data Collection				
Space group	$P6_5$ (170)	$I4_122$ (98)	$P6_4$ (172)	$P6_5$ (170)
Unit cell dimensions				
a, *b*, *c*; Å	114.15, 114.15, 120.62	71.06 71.06 145.67	211.24, 211.24, 53.16	125.16, 125.16, 88.54
α, *β*, *γ*; °	90, 90, 120	90, 90, 90	90, 90, 120	90, 90, 120
Molecules/A.U.	1	1	1 + 1 (1 complex)	1
Solvent content, %	57.8	66.9	67.6	56.8
Wilson B factor, Å^2	58.26	32.58	219	64.09
Resolution range, Å	45.7-2.42 (2.51-2.42)	41.4-1.87 (1.93-1.87)	51.1-4.45 (4.61-4.45)	28.5-2.70 (2.81-2.70)
Total reflections	113614 (11586)	90525 (8280)	81763 (8123)	70991 (7028)
Unique reflections	33737 (3337)	15763 (1396)	8634 (838)	21504 (2328)
Multiplicity	3.4 (3.5)	5.7 (5.9)	9.5 (9.7)	3.3 (3.0)
Completeness, %	99.0 (98.4)	99.4 (99.7)	99.7 (99.4)	98.4 (96.3)
Mean I/σ(I)	11.8 (1.3)	16.0 (1.4)	3.8 (0.5)	7.7 (0.7)
R_{pim}, %	4.6 (84.2)	3.3 (84.3)	12.0 (134.1)	6.2 (68.9)
CC(1/2), %	99.9 (54.1)	99.9 (52.8)	99.7 (25.9)	99.7 (46.3)
CC*, %	100.0 (83.8)	100.0 (83.1)	99.9 (64.1)	99.9 (79.5)
Refinement				
Reflections	33699 (3333)	15756 (1396)	8611 (833)	21434 (2319)
Free reflections	1636 (153)	1576 (139)	847 (70)	1140 (110)
R_{work}, %	22.58 (39.39)	21.77 (36.51)	28.61 (36.69)	23.38 (40.81)
R_{free}, %	26.33 (43.90)	23.59 (36.94)	31.83 (41.89)	27.02 (42.03)
CC_{work}, %	95.7 (67.4)	95.0 (68.9)	96.5 (50.0)	96.8 (61.3)
CC_{free}, %	94.5 (77.8)	93.8 (59.2)	90.3 (25.5)	93.7 (54.8)
ML coordinate error, Å	0.47	0.23	0.66	0.51
ML phase error, °	35.15	26.53	39.52	36.22
rmsd				
Bond lengths, Å	0.004	0.006	0.005	0.004
Bond angles, °	0.97	1.08	1.01	0.96
Ramachandran plot				
Favored, %	98.6	99.1	96.6	99.3
Allowed %	1.4	0.9	3.4	0.7
Outlier, %	0	0	0	0
Rotamer outliers, %	0.2	0	0.9	0.4
Clashscore	2.9	0.6	5.3	1.3
No of atoms				
Total	5210	901	5985	4626
Protein	5117	837	5934	4582
Ligand	67	12	51	29
Water	26	52	0	15
Protein residues	668	107	773	598
Average B factor, Å^2				
Total	76.6	51.4	256.0	84.8
Protein	76.5	51.5	256.1	85.0
Ligand	94.2	61.2	251.9	64.3
Water	47.7	48.5	-	71.8

Parameters for the outermost shell are shown in parentheses. A.U., asymmetric unit; CC(1/2), percentage of correlation between intensities from random half-datasets; CC*, √(2CC(1/2)/1+CC(1/2)); $CC_{\_}$, correlation of the experimental intensities of free reflections excluded from the refinement with the intensities calculated from the refined molecular model; $CC_{\_}$, correlation of the experimental intensities with the intensities calculated from the refined molecular model; DLS, Diamond Light Source; ESRF, European Synchrotron Radiation Facility; I/σI, signal-to-noise ratio; ML, maximum likelihood; $R_{\_}$, $\Sigma_{\_}$ √(1/n-1) Σ|Ii(hkl) - I(hkl)|/Σ Σ I(hkl), where I(hkl) is the intensity for an observation of a reflection and I(hkl) is the average intensity of all symmetry-related observations of a reflection; $R_{\_}$, $\Sigma_{\_}||F_{\_}| - k|F_{\_}||/\Sigma_{\_}|F_{\_}|$; $R_{\_}$, same as $R_{\_}$ calculated from free reflections excluded from refinement. Statistics were calculated using phenix.table_one, phenix.xtriage (solvent content) and phenix.refine (ML coordinate and phase errors).

SUPPLEMENTAL EXPERIMENTAL PROCEDURES

X-Ray Diffraction Data Collection

Datasets of ^{M}OR and ^{M}ZP were collected at 100 K at beamlines ID29 (de Sanctis et al., 2012) and ID23-1 (Nurizzo et al., 2006) of the European Synchrotron Radiation Facility (ESRF, Grenoble), equipped with PILATUS 6M-F detectors (Dectris). BMP9 and ^{M}OR-BMP9 complex datasets were collected at 100 K at beamline I02 of Diamond Light Source (DLS, Didcott), also equipped with a PILATUS 6M detector. Data was integrated and scaled with XDS (Kabsch, 2010), using high resolution data cutoffs chosen based on statistical indicators $CC_{1/2}$ and CC* (Evans and Murshudov, 2013; Karplus and Diederichs, 2015). Processing statistics are summarized in Table S1.

Structure Determination

The structure of ^{M}OR was solved by MR with Phaser (McCoy et al., 2007), using as search model an ensemble of MBP structures extracted from PDB entries 3SEX, 3SET (Laganowsky et al., 2011) and 4WRN (Bokhove et al., 2016a, 2016b). After autobuilding with PHENIX AutoBuild (Terwilliger et al., 2008) and manual building in Coot (Emsley et al., 2010), the model was refined using phenix.refine (Afonine et al., 2012). Protein and carbohydrate structure validation was performed with MolProbity (Chen et al., 2010) and Privateer (Agirre et al., 2015), respectively.

PDB entry 1ZKZ (Brown et al., 2005) was used to phase the data of BMP9 by MR. Rebuilding, refinement and validation were carried out as described for ^{M}OR.

The structure of the ^{M}OR-BMP9 complex was also determined by MR with Phaser. Despite the limited resolution of the dataset, correctness of the solution was indicated by a progressive decrease in refinement R-factors every time a new model component was added to the structure (Figure S4B). An independent indicator of the correct MR result was the placement of the BMP9 molecule in the unit cell which, together with 2-fold crystallographic symmetry, generated the known BMP9 homodimer (Brown et al., 2005) (Figures S4C and D). Due to the low resolution of the data, a conservative refinement strategy was followed, consisting of strictly constrained coordinate refinement together with group and translation, libration and screw (TLS) B-factor refinement (Winn et al., 2001), using one TLS group per domain.

MR of ^{M}ZP was performed using PDB entry 3SEX (Laganowsky et al., 2011) as a search model. After obtaining initial MR phases, density modification was carried out with RESOLVE (Terwilliger, 2004) in the PHENIX package (Adams et al., 2010). Model building was performed with Buccaneer (Cowtan, 2006) and Coot. Refinement and validation were performed as described for ^{M}OR.

Refinement statistics are summarized in Table S1.

Sequence and Structure Analysis

Sequence alignments were calculated using T-Coffee (Notredame et al., 2000) and compiled with ESPript (Robert and Gouet, 2014) or SeaView4 (Gouy et al., 2010).

The circular permutation of ENG OR was first recognized using Chimera (Pettersen et al., 2004). Superposition of OR1 and OR2 was performed using PDBefold (Krissinel and Henrick, 2005), which was also used to search for structural homologues of the OR domains.

PDBePISA analysis (Krissinel and Henrick, 2007) indicates that the interface between OR and BMP9 plays a significant role in complex formation (complex formation significance score (CSS) = 0.648). However, in both the OR and the OR-BMP9 structures the CSS of the interface between mMBP and OR is 0.000, indicating that there is no significant interface between the two moieties of the fusion protein. Furthermore, the packing of mMBP and OR is different between the liganded and unliganded state, which suggests that mMBP does not interfere with the structure of OR.

Solvent accessible area calculations and domain motion analysis were carried out with Naccess (Hubbard and Thornton, 1993) and DynDom (Hayward and Lee, 2002), respectively.

Figures were created with PyMOL (Schrödinger, LLC). The ENG surface in Figure 2C was colored according to the normalized consensus hydrophobicity scale (Eisenberg et al., 1984).

BLI Analysis of Protein-Protein Interaction

An Octet Red96 system (PALL FortéBio) was used to measure binding constants of recombinant human BMP9 (carrier free; R&D Systems) to purified ENG constructs and an mMBP control expressed in HEK293T cells (Figure S8H).

Before immobilization to High Precision Streptavidin (SAX) Dip and Read Biosensors (PALL FortéBio) hydrated in sample buffer (20 mM Na-HEPES pH 7.4, 150 mM NaCl, 0.05% Tween), BMP9 was biotinylated on ice for 2 hours and diluted to 5 µg/ml. Subsequently, sensors were blocked with biocytin (10 µg/ml) for 1 minute to avoid nonspecific binding. In order to calculate K_D, binding in the presence of increasing concentrations of each ENG construct (0 nM, 37.5 nM, 75 nM, 125 nM, 250 nM, 500 nM and 1 µM) was monitored. Two 60-second and 120-second baseline measurements were performed prior to association measurements. Association and dissociation were monitored during 240 and 300 seconds respectively. Nonspecific binding was monitored using a sensor not coated with BMP9 and ENG constructs at 125 nM concentration. Contribution of the buffer to the signal was measured with a BMP9-coated sensor. Both controls were subtracted from the binding signal in order to calculate K_D values.

SEC-MALS Analysis of the ENG-BMP9 Complex

The chromatographic system consisted of an HPLC system and autoinjector (Agilent 1260 Infinity, Agilent Technologies) coupled online with a MALS detector (miniDawn Treos, Wyatt Technology; 658 nm wavelength), a dRI detector (Optilab rEX, Wyatt

Technology; 658 nm wavelength) and a UV detector (Agilent 1260 Infinity, Agilent Technologies; 280 nm wavelength). Separation was performed by a Superdex 200 Increase 10/300 GL column (GE Healthcare), using a flow rate of 0.75 ml/min and a mobile phase consisting of 50 mM Na-HEPES pH 7.5, 25 mM KCl, 20 mM $MgCl_2$, 200 ppm NaN_3. Data processing and weight-averaged molecular mass calculation were performed using the ASTRA 7.0.2 software (Wyatt Technology).

SUPPLEMENTAL REFERENCES

Adams, P.D., Afonine, P.V., Bunkóczi, G., Chen, V.B., Davis, I.W., Echols, N., Headd, J.J., Hung, L.W., Kapral, G.J., Grosse-Kunstleve, R.W., et al. (2010). PHENIX: a comprehensive Python-based system for macromolecular structure solution. Acta Crystallogr. D Biol. Crystallogr. *66*, 213–221.

Afonine, P.V., Grosse-Kunstleve, R.W., Echols, N., Headd, J.J., Moriarty, N.W., Mustyakimov, M., Terwilliger, T.C., Urzhumtsev, A., Zwart, P.H., and Adams, P.D. (2012). Towards automated crystallographic structure refinement with phenix.refine. Acta Crystallogr. D Biol. Crystallogr. *68*, 352–367.

Agirre, J., Iglesias-Fernandez, J., Rovira, C., Davies, G.J., Wilson, K.S., and Cowtan, K.D. (2015). Privateer: software for the conformational validation of carbohydrate structures. Nat. Struct. Mol. Biol. *22*, 833–834.

Chen, V.B., Arendall, W.B., Headd, J.J., Keedy, D.A., Immormino, R.M., Kapral, G.J., Murray, L.W., Richardson, J.S., and Richardson, D.C. (2010). MolProbity: all-atom structure validation for macromolecular crystallography. Acta Crystallogr. D Biol. Crystallogr. *66*, 12–21.

Cowtan, K. (2006). The Buccaneer software for automated model building. 1. Tracing protein chains. Acta Crystallogr. D Biol. Crystallogr. *62*, 1002–1011.

Cymerman, U., Vera, S., Karabegovic, A., Abdalla, S., and Letarte, M. (2003). Characterization of 17 novel endoglin mutations associated with hereditary hemorrhagic telangiectasia. Hum. Mutat. *21*, 482–492.

Eisenberg, D., Schwarz, E., Komaromy, M., and Wall, R. (1984). Analysis of membrane and surface protein sequences with the hydrophobic moment plot. J. Mol. Biol. *179*, 125–142.

Emsley, P., Lohkamp, B., Scott, W.G., and Cowtan, K. (2010). Features and development of Coot. Acta Crystallogr. D Biol. Crystallogr. *66*, 486–501.

Evans, P.R., and Murshudov, G.N. (2013). How good are my data and what is the resolution? Acta Crystallogr. D Biol. Crystallogr. *69*, 1204–1214.

Gouy, M., Guindon, S., and Gascuel, O. (2010). SeaView version 4: A multiplatform graphical user interface for sequence alignment and phylogenetic tree building. Mol Biol Evol *27(2)*, 221–224.

Hayward, S., and Lee, R.A. (2002). Improvements in the analysis of domain motions in proteins from conformational change: DynDom version 1.50. J. Mol. Graph. Model. *21*, 181–183.

Hubbard, S.J., and Thornton, J.M. (1993). Naccess. Computer Program, Department of Biochemistry and Molecular Biology, University College London.

Kabsch, W. (2010). XDS. Acta Crystallogr. D Biol. Crystallogr. *66*, 125–132.

Karplus, P.A., and Diederichs, K. (2015). Assessing and maximizing data quality in macromolecular crystallography. Curr. Opin. Struct. Biol. *34*, 60–68.

Krissinel, E., and Henrick, K. (2005). Multiple alignment of protein structures in three dimensions. In Computational Life Sciences, M. R. Berthold, R. C. Glen, K. Diederichs, O. Kohlbacher, and I. Fischer, eds. (Springer Berlin Heidelberg), pp. 67–78.

Krissinel, E., and Henrick, K. (2007). Inference of macromolecular assemblies from crystalline state. J. Mol. Biol. *372*, 774–797.

Laganowsky, A., Zhao, M., Soriaga, A.B., Sawaya, M.R., Cascio, D., and Yeates, T.O. (2011). An approach to crystallizing proteins by metal-mediated synthetic symmetrization. Protein Sci. *20*, 1876–1890.

McCoy, A.J., Grosse-Kunstleve, R.W., Adams, P.D., Winn, Storoni, L.C., and Read, R.J. (2007). Phaser crystallographic software. J. Appl. Crystallogr. *40*, 658–674.

Notredame, C., Higgins, D.G., and Heringa, J. (2000). T-Coffee: A novel method for fast and accurate multiple sequence alignment. J. Mol. Biol. *302*, 205–217.

Nurizzo, D., Mairs, T., Guijarro, M., Rey, V., Meyer, J., Fajardo, P., Chavanne, J., Biasci, J.C., McSweeney, S., and Mitchell, E. (2006). The ID23-1 structural biology beamline at the ESRF. J. Synchrotron Radiat. *13*, 227–238.

Pettersen, E.F., Goddard, T.D., Huang, C.C., Couch, G.S., Greenblatt, D.M., Meng, E.C., and Ferrin, T.E. (2004). UCSF Chimera—a visualization system for exploratory research and analysis. J. Comput. Chem. *25*, 1605–1612.

Robert, X., and Gouet, P. (2014). Deciphering key features in protein structures with the new ENDscript server. Nucleic Acids Res. *42*, W320–W324.

de Sanctis, D., Beteva, A., Caserotto, H., Dobias, F., Gabadinho, J., Giraud, T., Gobbo, A., Guijarro, M., Lentini, M., Lavault, B., et al. (2012). ID29: a high-intensity highly automated ESRF beamline for macromolecular crystallography experiments exploiting anomalous scattering. J. Synchrotron Radiat. *19*, 455–461.

Terwilliger, T. (2004). SOLVE and RESOLVE: automated structure solution, density modification and model building. J. Synchrotron Radiat. *11*, 49–52.

Terwilliger, T.C., Grosse-Kunstleve, R.W., Afonine, P.V., Moriarty, N.W., Zwart, P.H., Hung, L.W., Read, R.J., and Adams, P.D. (2008). Iterative model building, structure refinement and density modification with the PHENIX AutoBuild wizard. Acta Crystallogr. D Biol. Crystallogr. *64*, 61–69.

Winn, Isupov, M.N., and Murshudov, G.N. (2001). Use of TLS parameters to model anisotropic displacements in macromolecular refinement. Acta Crystallogr. D Biol. Crystallogr. *57*, 122–133.